

# Potential for downscaling soil moisture maps derived from spaceborne imaging radar data

Wade T. Crow and Eric F. Wood

Department of Civil and Environmental Engineering, Princeton University, Princeton, New Jersey

Ralph Dubayah

Department of Geography, University of Maryland, College Park, Maryland

**Abstract.** The presence of nonlinear relationships between surface soil moisture and various hydrologic processes suggests that grid-scale water and energy fluxes cannot be accurately modeled without subgrid-scale soil moisture information. For land surface and energy balance models run over continental- to global-scale domains, accurate fine-scale soil moisture observations are nearly impossible to obtain on a consistent basis and will likely remain so through the next generation of soil moisture remote sensors. In the absence of such data sets, an alternative approach is to generalize the statistical behavior of soil moisture fields across the relevant range of spatial scales. Downscaling procedures offer the possibility that the fine-scale statistical properties of soil moisture fields can be inferred from coarse-scale data. Such an approach was used for a 29 x 200 km transect of 25 m active radar data acquired over Oklahoma by NASA's spaceborne imaging radar (SIR-C) mission on April 12, 1994. Using a soil dielectric inversion model, the radar data were processed to provide estimates of surface soil dielectric values, which can be equated to volumetric soil moisture content. The soil moisture field along each strip was analyzed for evidence of spatial scaling for scales ranging from 100 to 6400 m. Results suggest that a spatial scaling assumption may not always be an appropriate basis for a downscaling approach. Prospects for the development of a more robust downscaling procedure for soil moisture are discussed.

## 1. Introduction

Recent advances in surface soil moisture remote sensing have resulted in the possibility that such observations can be directly assimilated into weather prediction models. The crucial barrier to such an integration is the relatively coarse temporal and spatial scales at which remote sensors are likely to provide information about surface soil moisture conditions. Coarse temporal resolutions can be smoothed by running a water balance model in the interim between soil moisture image acquisition [Houser *et al.*, 1998]. Extracting soil moisture information at spatial scales finer than a sensor's resolution is more difficult. However, past studies by Dubayah *et al.* [1996] and Rodriguez-Iturbe *et al.* [1995] have shown that at scales of 100 to 1600 m, soil moisture fields may self-organize in such a way that their coarse-scale statistical properties provide information about variability at finer scales. Following the definitions of Blöschl and Sivipalan [1995], such a statistical inference is referred to as "downscaling" statistical information from coarse- to fine-scales.

The presence of nonlinear relationships between soil moisture and hydrologic processes such as evapotranspiration, infiltration, and recharge suggests that grid-scale results in land-atmosphere models will be sensitive to the presence or absence of subgrid-scale soil moisture variability. Results by

Wood [1997] demonstrate the sensitivity of grid-scale transpiration results to subgrid-scale soil moisture variability, while Avissar and Pielke [1989] have shown that land surface heterogeneity can have a significant effect on grid-scale circulation, surface temperature, and surface energy flux patterns in coupled land-atmosphere models.

This paper will explore the development of a downscaling procedure for surface soil moisture using data collected from the spaceborne imaging radar (SIR-C) L band sensor. A robust downscaling model would allow for estimates of subgrid-scale variability in soil moisture fields to be made based solely on grid-scale information. These estimates could, in turn, be used as the basis for a statistical-dynamical representation of subgrid soil moisture variability using a model structure similar to that presented by Famiglietti and Wood [1994] and Avissar [1992]. In this way, incorporation of subgrid statistical information can provide closure for the effects of nonresolved soil moisture variability and improve predictions of grid-scale water and energy fluxes.

## 2. Motivation for Downscaling

Nonlinear relationships between soil moisture and various hydrologic processes motivate the need for subgrid-scale soil moisture information.

For example, the relationship between canopy transpiration  $T$ , surface soil moisture  $\theta$ , and potential evapotranspiration  $E_p$ , is often modeled in a piecewise linear fashion [see, e.g., Federer, 1979] as

$$\begin{aligned}
 T &= 0, & \theta < \theta_w \\
 T &= E_p \left( \frac{\theta - \theta_w}{\theta_c - \theta_w} \right), & \theta_w < \theta < \theta_c \\
 T &= E_p, & \theta_c < \theta.
 \end{aligned} \quad (1)$$

The discontinuities in this function at the wilting point  $\theta_w$  and the critical soil moisture  $\theta_c$  give it a nonlinear structure.

Bare soil evaporation has been parameterized by means of a physical transport resistance in the presence of soil moisture or soil water vapor gradients. This resistance to evaporation  $r_{\text{soil}}$  is often expressed as a nonlinear function of soil moisture. *Van de Griend and Owe* [1994] give the relationship as

$$r_{\text{soil}} = 10 \exp [35.6 (0.15 - \theta)]. \quad (2)$$

Finally, a standard Brooks-Corey formulation predicts a nonlinear relationship between soil moisture and relative hydraulic conductivity  $K_{\text{rel}}$

$$K_{\text{rel}} = K_{\text{sat}} \left( \frac{\theta - \theta_r}{\theta_{\text{sat}} - \theta_r} \right)^{\frac{2+3m}{m}}, \quad (3)$$

where  $m$  is the pore size distribution index,  $\theta_r$  is the residual soil moisture,  $\theta_{\text{sat}}$  is the saturated soil moisture, and  $K_{\text{sat}}$  is the conductivity at soil saturation. Any water balance model that incorporates this formulation will be nonlinear with respect to soil moisture.

As a consequence of these nonlinearities, the loss of sub-grid information due to the imaging of soil moisture fields at coarse grid-scale resolutions will likely impact grid aggregated model output, especially during periods of soil moisture controlled evapotranspiration. Downscaling procedures offer the promise of recovering subgrid soil moisture information and correcting for the effects of its omission.

### 3. Statistical Downscaling Model

The simplest form for a downscaling procedure is to assume that soil moisture fields self-organize in a way such that no distinct length scales can be identified. A given two-dimensional field  $\Phi$  is said to exhibit "spatial scaling" if

$$E(\Phi_\lambda^q) = \left( \frac{\lambda}{\lambda_{\text{max}}} \right)^{K_q} E(\Phi_{\lambda_{\text{max}}}^q), \quad (4)$$

where  $E(\Phi_\lambda^q)$  is the  $q$ th statistical moment of the field resolved at scale  $\lambda$ , and  $\lambda_{\text{max}}$  is an arbitrary reference scale usually taken to be the coarsest scale available [*Gupta and Waymire*, 1990].

For the case  $q = 2$  (i.e., the second moment) the natural log of (4) becomes

$$\ln [E(\Phi_\lambda^2)] = K_2 \ln \left( \frac{\lambda}{\lambda_{\text{max}}} \right) + \ln [E(\Phi_{\lambda_{\text{max}}}^2)]. \quad (5)$$

In this analysis the field  $\Phi$  is defined to be field of anomalies around the mean within the field  $\Psi$ . Therefore (5) is equivalent to

$$\ln [\text{Var}(\Psi_\lambda)] = K_2 \ln \left( \frac{\lambda}{\lambda_{\text{max}}} \right) + \ln [\text{Var}(\Psi_{\lambda_{\text{max}}})]. \quad (6)$$

When transformed into log-log space, plots of  $\text{Var}(\Psi_\lambda)$  versus  $\lambda/\lambda_{\text{max}}$  will be referred to as "scaling plots." The log-log slope  $K_2$  will be called the "scaling exponent." In this paper, the term "spatial scaling" will be used to describe fields in which (6) holds.

The magnitude of the scaling exponent can be taken as a measure of the correlation among neighboring pixels in a field. Zero spatial correlation corresponds to a case where neighboring pixels are statistically independent. If these statistically independent neighboring pixels are aggregated to form a second image at a coarser resolution than the original image, the decrease in variability that accompanies the image aggregation can be predicted from the central limit theorem. Specifically, the variance of the new coarsely resolved field  $\Psi_{\lambda_{\text{coarse}}}$  can be calculated as

$$\text{Var}(\Psi_{\lambda_{\text{coarse}}}) = \frac{\text{Var}(\Psi_\lambda)}{n_{\lambda, \lambda_{\text{coarse}}}}, \quad (7)$$

where  $n_{\lambda, \lambda_{\text{coarse}}}$  is the number of subpixels at the original fine pixel scale  $\lambda$  that are contained within a single coarse-scale ( $\lambda_{\text{coarse}}$ ) pixel. For a two-dimensional field

$$n_{\lambda, \lambda_{\text{coarse}}} = \left( \frac{\lambda_{\text{coarse}}}{\lambda} \right)^2, \quad (8)$$

therefore (7) can be rewritten as

$$\text{Var}(\Psi_\lambda) = \text{Var}(\Psi_{\lambda_{\text{max}}}) \left( \frac{\lambda_{\text{coarse}}}{\lambda} \right)^2. \quad (9)$$

Rewriting (9) in the form of (6) and assigning  $\lambda_{\text{coarse}}$  to be  $\lambda_{\text{max}}$  yields

$$\ln [\text{Var}(\Psi_\lambda)] = -2 \ln \left( \frac{\lambda}{\lambda_{\text{max}}} \right) + \ln [\text{Var}(\Psi_{\lambda_{\text{max}}})]. \quad (10)$$

The case of zero spatial correlation among neighboring pixels corresponds to a scaling plot with a scaling exponent ( $K_2$ ) of  $-2$ . In contrast, if neighboring pixels are perfectly correlated over all scales, then no variability is lost during each aggregation step, resulting in a scaling plot with a log-log slope of zero.

In general, the degree to which neighboring pixels are correlated can vary as a function of scale. However, a property of spatially scaling fields is that the correlation of neighboring pixels is independent of resolution (scale), and a single scaling exponent can be fitted to log-log plots of variance versus scale.

If a single scaling exponent can be fitted over a range of scales, then it should be possible to estimate the scaling exponent  $K_2$  using only coarse-scale data and use that value to extrapolate down to finer scales. The purpose of the analysis presented in this paper is to determine whether a fitted value of  $K_2$ , derived from grid-scale remotely sensed soil moisture data, can be used to describe the spatial autocorrelation structure of soil moisture at subgrid-scales.

### 4. Application to Remote Sensing Data

Soil moisture patterns are imposed on landscapes by processes that operate at a wide range of length scales. Hydrologic processes (infiltration, evapotranspiration, and runoff) and variability in soil properties occur at spatial scales of the

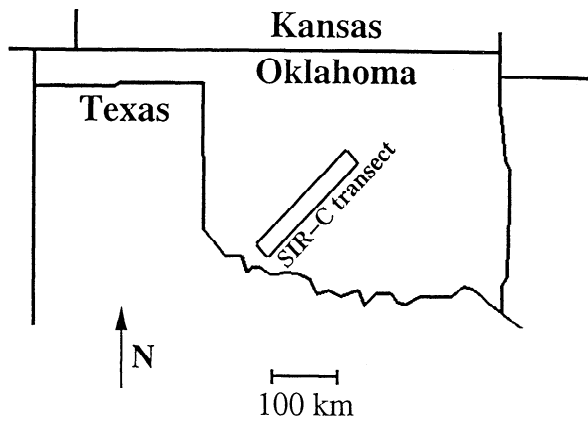


**Figure 1.** Location of the April 12, 1994 SIR-C transect in southeastern Oklahoma. The transect center is located at  $34^{\circ} 53.9' N$  and  $98^{\circ} 2.9' W$ . The transect follows a line  $41.1^{\circ}$  East of North and has dimensions of  $199.9 \text{ km} \times 28.9 \text{ km}$ .

order 10-1000 m, while atmospheric inputs (precipitation and radiative forcings) occur at scales of  $10^2$  to  $10^5$  m [Wood, 1998]. As a result, understanding the spatial structure of soil moisture fields requires soil moisture information at a wide range of scales. Soil moisture maps derived from radar remote sensing sources have the potential to meet this need. Unfortunately, this potential has not yet been fully met. The availability of data sets with both large spatial coverage and fine spatial resolution is currently limited to observations from NASA's spaceborne imaging radar (SIR-C). These observations provide a unique view of the scaling behavior of soil moisture fields at scales ranging from tens of meters to hundreds of kilometers.

#### 4.1. Description of Remote Sensing Data Set

The first SIR-C mission lasted 12 days from April 4 to 16, 1994. On April 12 a transect centered over the  $525 \text{ km}^2$  Little Washita Basin in southwest Oklahoma was acquired; see Figure 1. The transect stretched over 200 km from the southwest corner of Oklahoma to the outer reaches of Oklahoma City. Other April 12 transects of the region were processed but were omitted from this analysis due to the presence of heavy vegetation which made accurate recovery of soil moisture information difficult.

The SIR-C system is capable of emitting and receiving horizontally and vertically polarized signals at X, C, and L bands. As a result, the following send and receive backscatter polarization orientations are possible:  $\sigma_{HH}$ ,  $\sigma_{VV}$ ,  $\sigma_{HV}$ , and  $\sigma_{VH}$ . Backscatter imagery was made available at a resolution of 25 m.

The SIR-C backscatter transect shown in Figure 2a has a number of attributes that make it an ideal data source for the study of soil moisture spatial scaling properties. These attributes include an L band wavelength (24 cm) which is long enough to penetrate lightly vegetated canopies [Ulaby *et al.*, 1979], the availability of multiple polarization information which facilitates the isolation of surface roughness [Jackson *et al.*, 1997], and an extremely large scene size to resolution ratio (200 km versus 25 m) which captures the statistical properties of soil moisture fields over a wide range of scales.

Coincident rainfall information at 4 km is available from National Oceanic Atmospheric Administration Weather Surveillance Radar (WSR-88D) rainfall imagery of the region. The week preceding the data acquisition on April 12, 1994 was dry, except for a rain event on April 11. Rainfall accumulations for the April 11 event are shown in Figure 2b.

#### 4.2. Estimation of Soil Dielectric From Radar Backscatter

The interaction of active radar signals with the land surface is affected by surface roughness, vegetation, and the dielectric properties of the soil. To invert the backscatter images into soil dielectric values, the model of Dubois *et al.* [1995] was applied to the 25 m L band SIR-C data. The model gives the transformation from  $\sigma_{HH}$  and  $\sigma_{VV}$  backscatter cross-sections to surface roughness height  $h$  and soil dielectric  $\epsilon$  as

$$\sigma_{VV} = 10^{-2.75} \frac{\cos^3(\eta)}{\sin^3(\eta)} 10^{0.046\epsilon \tan(\eta)} [kh \sin(\eta)]^{1.1} \alpha^{0.7} \quad (11)$$

$$\sigma_{HH} = 10^{-2.75} \frac{\cos^{1.5}(\eta)}{\sin^5(\eta)} 10^{0.028\epsilon \tan(\eta)} [kh \sin(\eta)]^{1.4} \alpha^{0.7},$$

where  $\eta$  is the sensor incidence angle,  $\alpha$  is the radar wavelength, and  $k$  is the wave number of the radar. If both  $\sigma_{HH}$  and  $\sigma_{VV}$  are known, then (11) can be solved simultaneously for  $h$  and  $\epsilon$ .

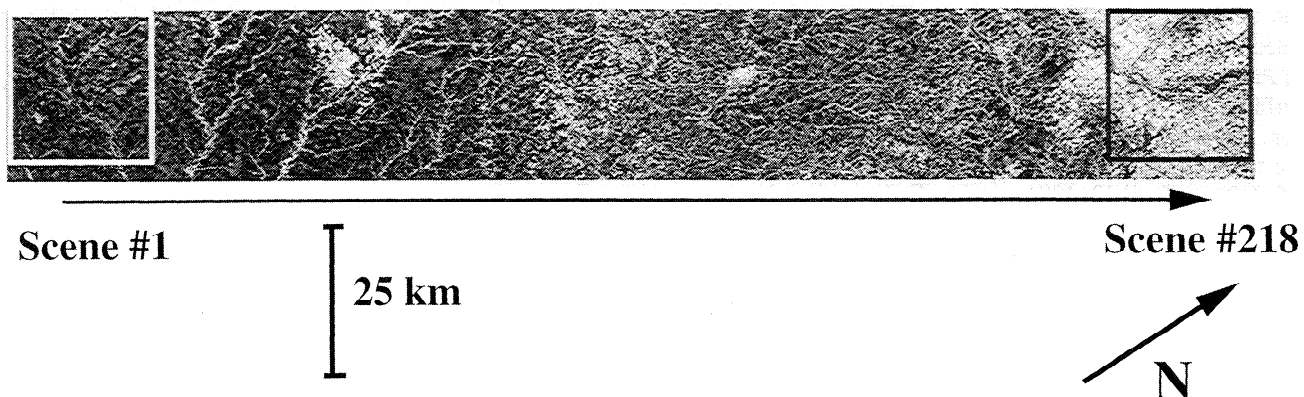


**Figure 2a.** A backscatter image of the transect. The moving window is slid along the length of the transect at 800 m increments to define 218 distinct  $25.6 \times 25.6 \text{ km}$  scenes.

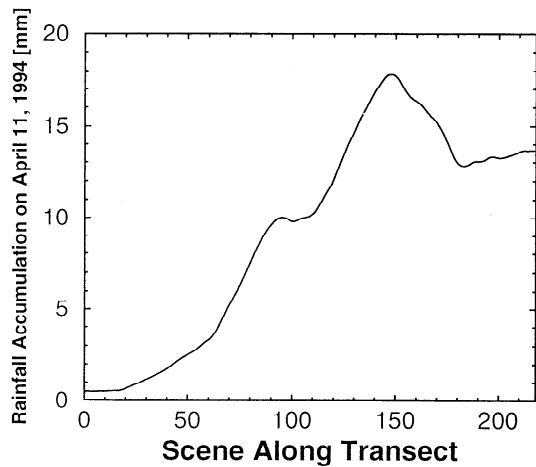


**Figure 2b.** Rainfall accumulations in the 24 hour period preceding image acquisition.

Wang *et al.* [1997] evaluated the Dubois *et al.* [1995] model, as well a similar model presented by Shi *et al.* [1997], over the Little Washita Basin. They concluded that the Dubois *et al.* [1995] model was capable of estimating soil moisture for bare and sparsely vegetated fields within a standard error of  $\sim 0.06 \text{ cm}^3/\text{cm}^3$ . The performance of both models was degraded when applied to fields with moderate to heavy amounts of vegetation. This degradation was especially acute for the Shi *et al.* [1997] algorithm, which appeared to break down over areas covered with even short vegetation [Wang *et al.*, 1997].

Dubois *et al.* [1995] uses the cross-polarization ratio  $\sigma_{HV}/\sigma_{VH}$  to identify pixels that are too heavily vegetated for inversion using (11). They suggest a masking criteria of

$$\frac{\sigma_{HV}}{\sigma_{VH}} < -11 \text{ dB} \quad (12)$$

to remove heavily vegetated pixels from radar imagery. The ratio correlates well with vegetative indices. The value of -11 dB used as a threshold in (12) corresponds to a normalized difference vegetation index (NDVI) of about 0.4 [Dubois *et al.*, 1995]. Backscatter signals in pixels that fail this criteria are likely to be dominated by scattering off vegetation and contain less information about underlying soil moisture conditions.

Typical land cover conditions for pixels that satisfy (12) can be assessed through comparison with other more sophisticated vegetation classifications. For instance, the algorithm of Pierce *et al.* [1994] uses multispectral radar data to classify surfaces as bare soil, short vegetation, tall vegetation, and urban. Over the Little Washita Basin (located at the center of the transect) approximately 80% of the 25 m pixels that satisfy (12) on April 12, 1994 are classified as either short vegetation or bare soil by the Pierce *et al.* [1994] algorithm.

In addition, thematic mapper satellite imagery from an overpass of the region on April 12, 1994, provides an opportunity to compare NDVI values within the Little Washita Basin to SIR-C radar data acquired on the same day. Figure 3 shows a histogram of NDVI values for pixels that pass the criteria described in (12). Nearly 90% of these pixels satisfy the 0.4 NDVI threshold cited by Dubois *et al.* [1995] as the upper bound for the application of their model. Taken to-

gether, results from the Pierce *et al.* [1994] algorithm and the thematic mapper NDVI measurements suggest that pixels within the transect satisfying (12) can generally be characterized as covered by short, sparse vegetation.

#### 4.3. Estimation of Soil Moisture From Soil Dielectric

Soil dielectric properties in the microwave spectral region are strongly correlated to soil moisture. For L band, Hallikainen *et al.* [1985] gives the empirical relationship between the volumetric soil moisture  $\theta_v$  and soil dielectric  $\epsilon$  as

$$\begin{aligned} \epsilon = & [19.006 - 0.5(\% \text{ sand}) + 0.633(\% \text{ clay})] \theta_v^2 \\ & + [3.803 + 0.462(\% \text{ sand}) - 0.341(\% \text{ clay})] \theta_v \\ & + [2.862 - 0.012(\% \text{ sand}) + 0.001(\% \text{ clay})]. \end{aligned} \quad (13)$$

While it is clear that soil dielectric values are highly sensitive to surface soil moisture conditions, (13) suggests they also vary as a function of a soil's sand and clay content. The role of soil texture in the relationship between soil dielectric and soil moisture appears to be unresolved. Brisco *et al.* [1992] found no significant soil texture effects on the relationship between L band soil dielectric results and volumetric soil moisture. Their empirical expression relates soil moisture to soil dielectric and contains no reference to soil texture

$$\begin{aligned} \theta_v = & -2.78 \times 10^{-2} + 2.80 \times 10^{-2} \epsilon \\ & - 5.86 \times 10^{-4} \epsilon^2 + 5.03 \times 10^{-6} \epsilon^3. \end{aligned} \quad (14)$$

Using a truck-mounted radar, Dubois *et al.* [1995] found that relationships between soil dielectric and soil moisture varied by a maximum of 1% for a range of soil textures. Similar work by Jackson [1990] reached the same conclusion. In contrast to Hallikainen *et al.* [1985], these results suggest that soil texture has a small, if not negligible, role in adding variability to soil dielectric fields.

#### 4.4. Processing for Scaling Analysis

Using the model of Dubois *et al.* [1995] (equation (11)), the SIR-C backscatter transect data were processed into estimates of soil dielectric constants. Two separate volumetric soil moisture images were then created: one using the Brisco *et al.* [1992] (equation (14)) model and the other based on the

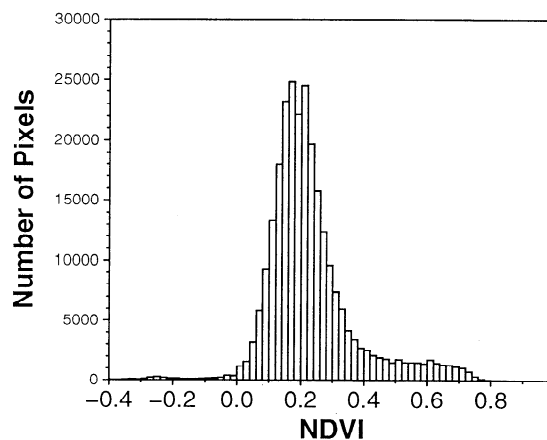


**Figure 3.** Histogram of NDVI values for pixels that pass the criteria described in (12).

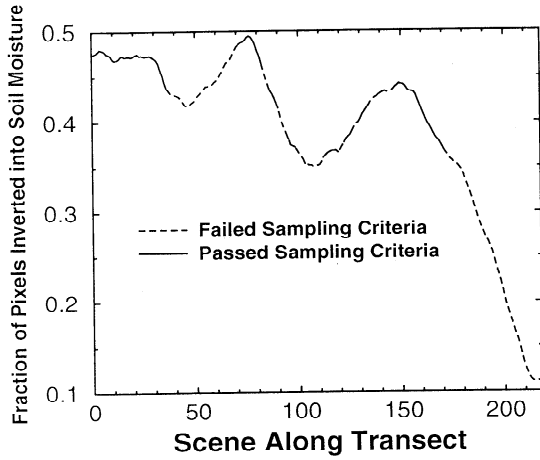


**Figure 4.** Fraction of pixels per scene that can be inverted into soil moisture estimates. Scenes with dotted results were deemed to be inadequately sampled and subsequently dropped from the analysis.

model of *Hallikainen et al.* [1985] (equation (13)). A 1 km soil map derived from the State Soil Geographic (STATSGO) data base provided the clay and sand fractions required by (13).

Once inversion into soil moisture was complete, a 25.6 km by 25.6 km moving window was passed along the length of the two soil moisture transects at increments of 800 m. At every increment a 1024 by 1024 pixel window was defined. As illustrated in Figure 2a, along the length of the transect there are 218 possible positions for this window. Each window (or scene) contained a number of 25 m pixels that either failed to meet the criteria established in (12) or returned dielectric values that could not be converted into soil moisture values [*Wang et al.*, 1997]. Figure 4 plots the fraction of each scene that could be fully processed into soil moisture.

The fact that these fields contained masked pixels and had a dimension less than 2 introduced a level of ambiguity into attempts to measure their variability at scales coarser than 25 m. Previous studies by *Dubayah et al.* [1996] and *Rodriguez-Iturbe et al.* [1995] resolved this issue by removing from their analyses every coarse-scale pixel that contained any masked subgrid area. The highly processed airborne remote sensing imagery they used allowed them to do this and still retain a sufficient sample of coarse-scale pixels from which to estimate coarse-scale variances. Adoption of a similar policy for the SIR-C data set would severely restrict the range of spatial scales that could be examined.

Instead, an alternative approach based on statistical sampling theory was developed. The procedure separates the soil moisture field  $\Psi$  into its mean and perturbation components. The variance of the field  $\Psi$  can then be written as follows

$$\text{Var}(\Psi) - \text{Var}(\Psi') = \text{Var}(\bar{\Psi}), \quad (15)$$

where  $\Psi$  represents the random field,  $\bar{\Psi}$  is the coarse-scale mean of the field, and  $\Psi'$  is the local perturbation around the coarse-scale mean.

Calculation of terms on the left-hand side of (15) is straightforward. The perturbation variance  $\text{Var}(\Psi')$  is the variance of the 25 m dielectric pixels around the local coarse-

scale pixel mean, while the fine-scale variance  $\text{Var}(\Psi)$  is the variance of the 25 m pixels around the scene-scale mean. Combined with (15), these two quantities provide a measure of the coarse-scale variance.

As an example, assign 800 m to be the coarse-scale. Within each 800 m pixel, estimated variances around the local 800 m mean and the scene-scale mean can be arrived at through sampling 25 m pixel values

$$(S_{\Psi'})_{800\text{m}} = \frac{N-1}{N} \left( \frac{\sum_{800\text{m}} \Psi_{25\text{m}}^2}{n-1} - \frac{\sum_{800\text{m}} \Psi_{25\text{m}}}{n-1} \frac{\sum_{800\text{m}} \Psi_{25\text{m}}}{n} \right) \quad (16)$$

$$(S_{\Psi})_{800\text{m}} = \sum_{800\text{m}} \frac{(\Psi_{25\text{m}} - \mu_{\Psi})^2}{n}, \quad (17)$$

where  $n$  is the sample size,  $N$  is the population size, and  $\mu_{\Psi}$  the mean of the entire scene. In (16),  $n$  is the number of unmasked 25 m pixels sampled within an 800 m pixel and  $N$  the total number of 25 m pixels in an 800 m pixel (1024). The sample size  $n$  will vary depending on the number of unmasked 25 m pixels remaining in each 800 m pixel. A “sampling criteria” can be defined that expresses the minimum fraction of fine-scale pixels that each coarse-scale pixel must contain in order to be included in the sampling. For this analysis it was set at 25%. This criteria sets a lower bound on acceptable values of  $n$ . The factor  $N-1/N$  is included in (16) to account for the effect of finite population sizes. Equation (17) describes sampling from an extremely large population (the  $2^{20}$  25 m pixels in each scene), so the factor is omitted. Likewise, the sample size is sufficiently large that the loss of a single degree of freedom due to the estimation of the scene-scale mean  $\mu_{\Psi}$  can be neglected in (17).

From statistical sampling theory, the distribution of these sampled variances is

$$(S_{\Psi'})_{800\text{m}} \sim \chi_{n-1}^2 \frac{\text{Var}(\Psi')_{800\text{m}}}{n-1} \quad (18)$$

$$(S_{\Psi})_{800\text{m}} \sim \chi_n^2 \frac{\text{Var}(\Psi)_{800\text{m}}}{n}, \quad (19)$$

where  $\chi^2$  is the chi-square distribution.

Averaging the sampled variances within each 800 m pixel over all the 800 m pixels contained in a scene yields

$$\overline{(S_{\Psi'})_{800\text{m}}} \cong \overline{\chi_{n-1}^2 \frac{\text{Var}(\Psi')_{800\text{m}}}{n-1}} = \text{Var}(\Psi') \quad (20)$$

$$\overline{(S_{\Psi})_{800\text{m}}} \cong \overline{\chi_n^2 \frac{\text{Var}(\Psi)_{800\text{m}}}{n}} = \text{Var}(\Psi) \quad (21)$$

Combing (20) and (21) with (15) gives

$$\overline{(S_{\Psi})_{800\text{m}}} - \overline{(S_{\Psi'})_{800\text{m}}} \cong \text{Var}(\bar{\Psi}). \quad (22)$$

Equation (22) allows for the estimation of an 800 m scale variance (i.e., a coarse-scale variance) based on a sampling of 25 m pixel values. As a result, 800 m pixels that contain missing 25 m pixels can be included in the analysis. The estimated variances will contain sampling error; however, individual sampling errors mutually cancel as the sampled vari-

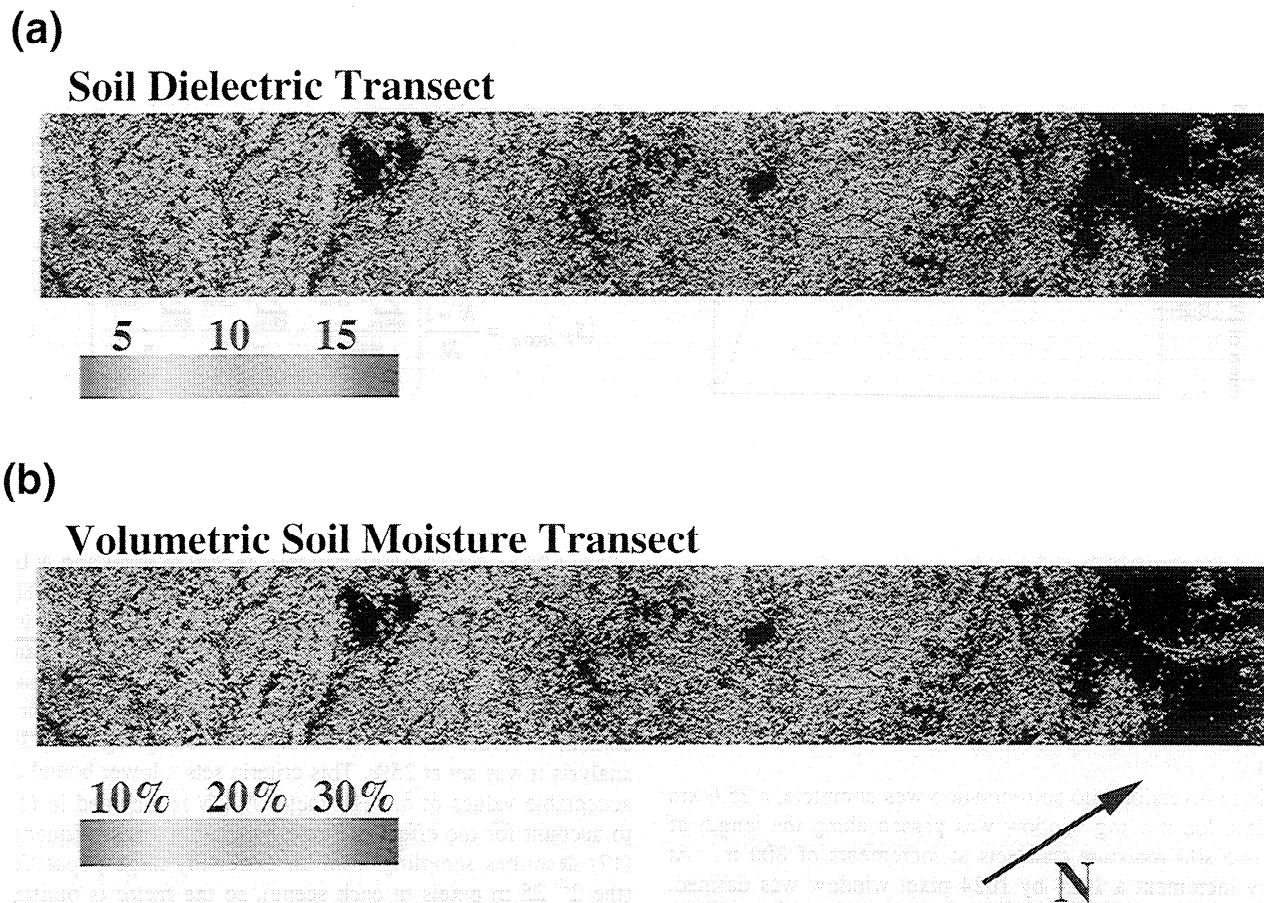


**Figure 5.** (a) Image of the soil dielectric field estimated along the transect using the *Dubois et al.* [1995] model. Black areas are surfaces that were masked out of the analysis due to excessive vegetation. (b) Image of soil moisture field estimated along the transect by applying the *Hallikainein et al.* [1985] model to results of the *Dubois et al.* [1995] model.

ances within each 800 m pixel are averaged over the entire scene.

For each scene in the transect, backscatter, soil dielectric, and soil moisture variances at scales of 100, 200, 400, 800, 1600, 3200, and 6400 m were estimated using the sampling procedure outlined in (22). To ensure adequate spatial sampling and to remove any ambiguity in the results due to masking, scaling plots were constructed only for scenes in which all sixteen 6400 m pixels met the 25% sampling criteria. The location of scenes where spatial sampling was deemed inadequate is shown in Figure 3. Variances at scales finer than 100 m were considered compromised by speckle contamination and not analyzed. For this analysis, scales coarser than 800 m will be referred to as “coarse-scale” and those finer than 800 m as “fine-scale.”

## 5. Results

Spatial scaling may be observed in a linear relationship between log resolution and log variance. If the spatial correlation structure of soil moisture fields can be accurately modeled with such a relationship, then the statistical structure of fine-scale soil moisture fields can be inferred from coarse-scale data.

### 5.1. Results of Soil Moisture and Soil Dielectric Inversion

The soil dielectric field estimated by the *Dubois et al.* [1995] algorithm is shown in Figure 5a. Scene averaged values for estimated surface roughness  $kh$  and soil dielectric  $\epsilon$  fields are shown in Figures 6a and 6b. The sliding window illustrated in Figure 2a defines each scene. *Dubois et al.* [1995] suggests that their inversion performs optimally over natural surfaces with  $kh < 2.5$ . This condition is met over the entire length of the transect.

Figure 5b shows the soil moisture field calculated by applying the *Hallikainein et al.* [1985] model (equation (13)) to the soil dielectric field shown in Figure 5a. Figure 6c shows scene averaged soil moisture values along the transect, based on soil moisture values estimated by both the *Hallikainein et al.* [1985] and *Brisco et al.* [1992] (equation (14)) models. The observed spatial trend in the soil moisture field estimated by the *Brisco et al.* [1992] model tends to reflect recent rainfall accumulations (see Figure 2b). The correlation between rainfall accumulations and soil moisture is weaker for the *Hallikainein et al.* [1985] results.

### 5.2. Performance of Spatial Scaling Model

The soil moisture fields estimated from both the *Brisco et al.* [1992] and *Hallikainein et al.* [1985] models were ana-

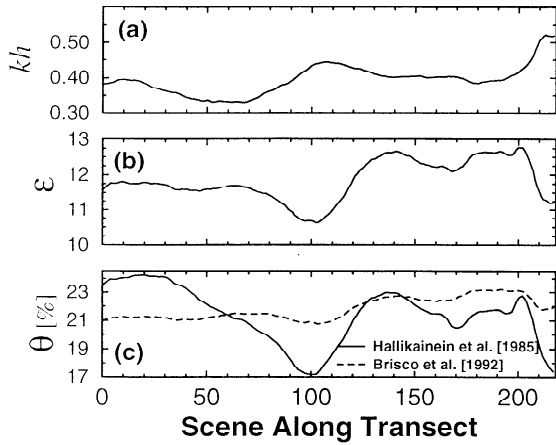


**Figure 6.** Scene averaged values of (a) surface roughness  $kh$ , (b) soil dielectric  $\epsilon$ , and (c) volumetric soil moisture  $\theta$ .

lyzed for the presence of spatial scaling. Figure 7 shows a typical scaling plot calculated from an individual soil moisture scene. The linear nature of the log-log plot appears to support an assumption of spatial scaling for the field between the scales of 100 and 6400 m. Figure 8a displays calculated correlation coefficients ( $r^2$ ) for linear least square regression fits to scaling plots constructed from scenes along both of the soil moisture transects. The consistently large  $r^2$  values for the

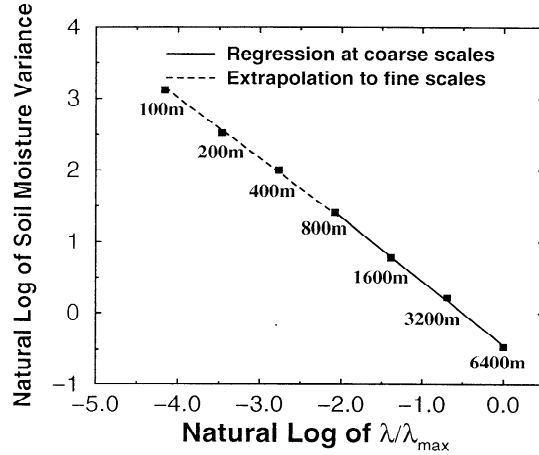


**Figure 7.** Scaling plot of a single soil moisture scene. The log-log linearity of the plot suggests that the field exhibits spatial scaling. Therefore a linear regression fit at coarse-scales combined with a linear extrapolation to fine-scales should be capable of recovering fine-scale statistical information [Dubayah et al., 1996].

linear fits suggest that the size of the scaling exponent does not vary significantly with scale; that is, the scenes display spatial scaling. This is especially true for the soil moisture field produced using the Brisco et al. [1992] model.

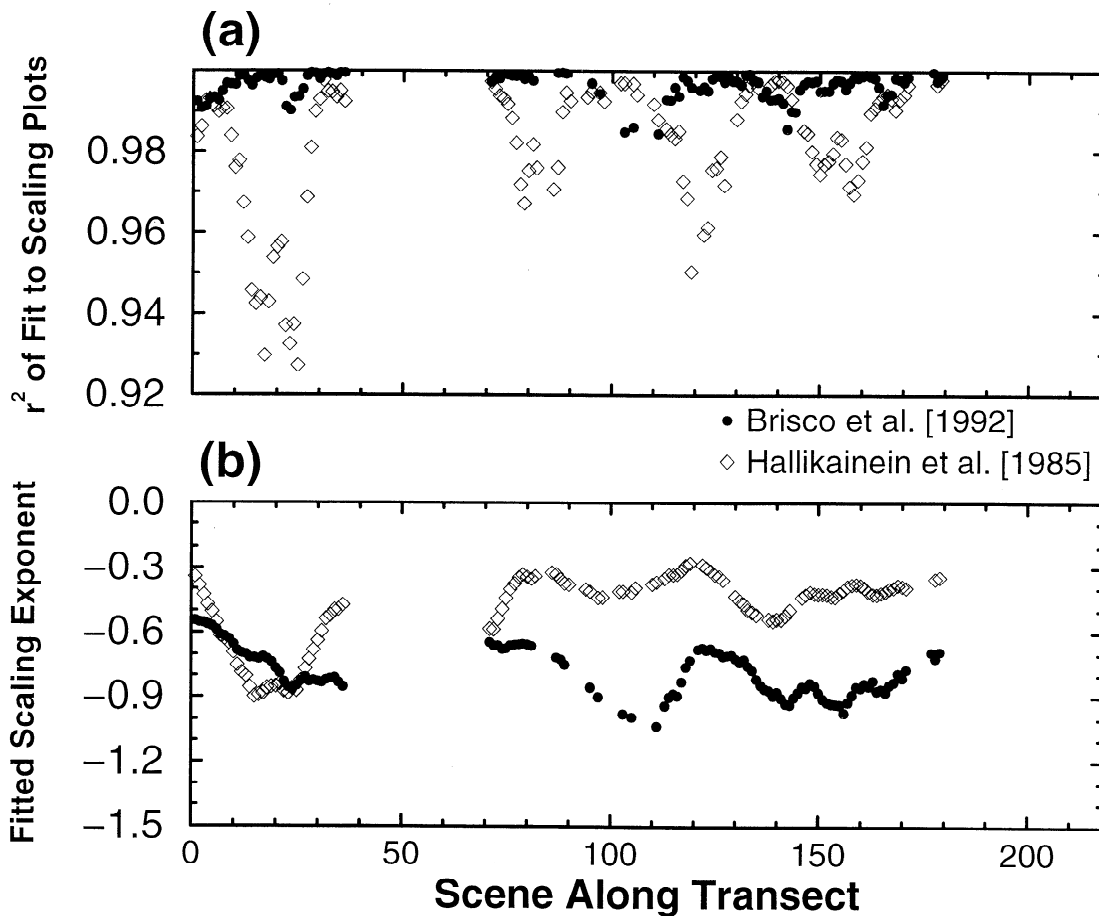


**Figure 8.** (a) Correlation coefficients and (b) scaling exponents for scaling plots constructed from scenes along the length of the Brisco et al. [1992] (solid circles) and the Hallikainein et al. [1985] (open diamonds) soil moisture transects.

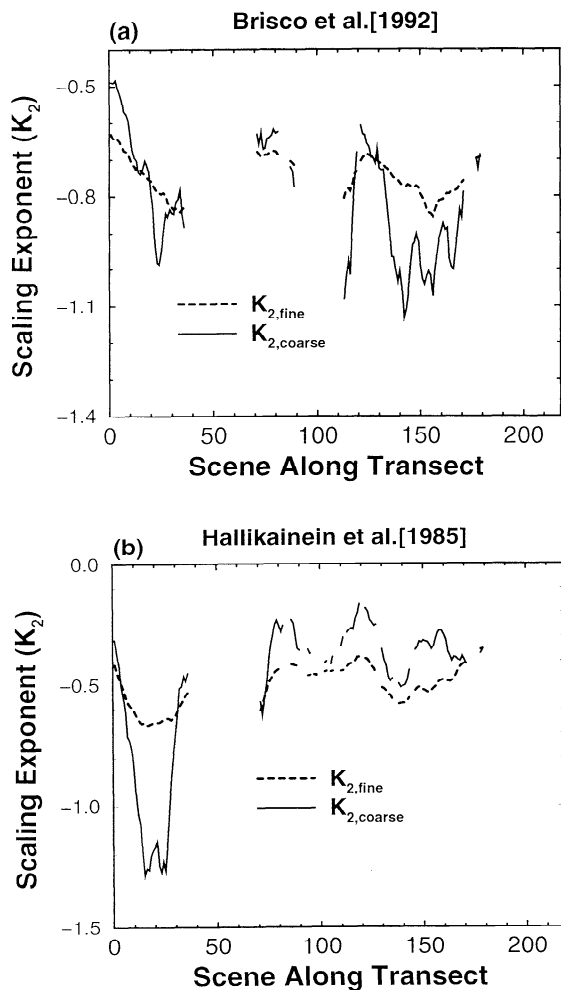


**Figure 9.** Comparison of  $K_{2,coarse}$  and  $K_{2,fine}$  along the (a) *Brisco et al.* [1992] and (b) *Hallikainein et al.* [1985] soil moisture transects.

According to (6), fitting slopes to log-log plots like Figure 7 is one method of estimating scaling exponents. Figure 8b plots 100 to 6400 m scaling exponents calculated within each scene of both soil moisture transects. Scaling exponents for the *Hallikainein et al.* [1985] model are less negative (less decrease in variability with scale) due to the inclusion of soil texture variability in the estimation of soil moisture. This soil texture variability reflected in the 1 km STATSGO soil texture map typically exhibits length scales larger than 6400 m. The inclusion of this large-scale variability reduces the relative magnitude of the soil moisture variability at length scales finer than 6400 m. Consequently, it leads to shallower log-log slopes (i.e., less negative scaling exponents) in scaling plots.

Taken together, Figures 7 and 8 suggest the following approach. Assume that a spatial scaling model accurately describes the correlation structure of the soil moisture field at scales of 100 to 6400 m. If this assumption holds, then a scaling exponent fit at coarse-scales (>800 m) can be accurately extrapolated down to fine-scales (<800 m) [*Dubayah et al.*, 1996]. Figure 7 illustrates the procedure. This will be referred to as the “spatial scaling model.” The model can be summarized as

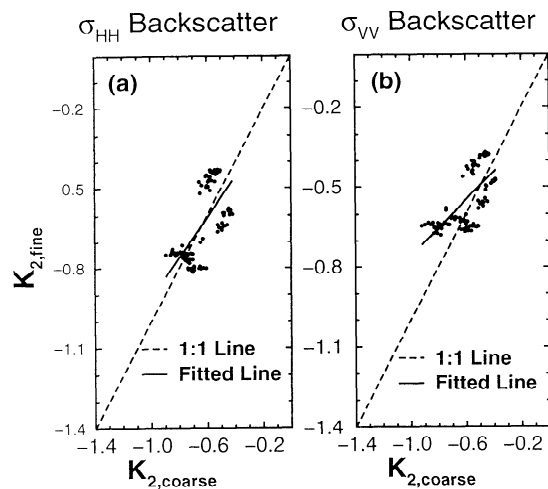


**Figure 10.** Scatter plot of  $K_{2,coarse}$  versus  $K_{2,fine}$  for backscatter scenes: (a)  $\sigma_{HH}$  and (b)  $\sigma_{VV}$ .

$$K_{2,fine} = K_{2,coarse} \quad (23)$$

where  $K_{2,coarse}$  is the scaling exponent fitted between 800 and 6400 m and  $K_{2,fine}$  is the exponent fitted between 100 and 800 m.

Figures 9a and 9b provide a more complete test of the spatial scaling model’s ability to provide accurate estimates at fine-scales. The figures plot  $K_{2,coarse}$  and  $K_{2,fine}$  for each scene along the length of both soil moisture transects. Gaps in the figures (scenes without results) were deemed to be inadequately sampled according to the criteria described in section 4.4 and subsequently dropped from the analysis. The results indicate that the spatial scaling model holds only approximately and that the departures can be quite large. The results presented in Figure 9 are summarized in scatterplots shown in Figures 12a and 12b. Figure 12 illustrates the existence of a significant correlation between coarse- and fine-scale scaling exponents for both models, but this correlation does not appear to follow the 1:1 ratio predicted by the spatial scaling model.

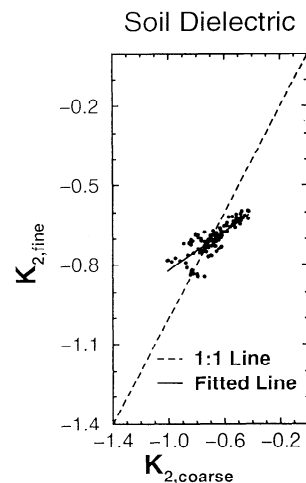


**Figure 11.** Scatter plot of  $K_{2,coarse}$  versus  $K_{2,fine}$  for soil dielectric ( $\epsilon$ ) scenes.

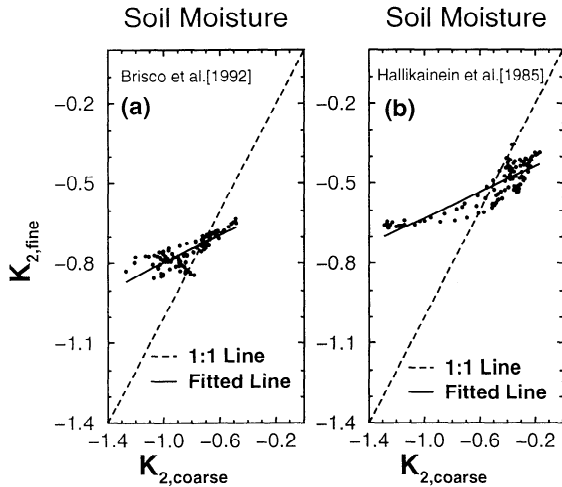


**Figure 12.** Scatter plot of  $K_{2,coarse}$  versus  $K_{2,fine}$  for soil moisture ( $\theta$ ) scenes: (a) *Brisco et al.* [1985] and (b) *Hallikainein et al.* [1985].

### 5.3. Evolution of Scaling Behavior During Data Processing

Figure 12 suggests two features govern the scaling behavior of soil moisture fields between the scales of 100 and 6400 m: a positive correlation between  $K_{2,coarse}$  and  $K_{2,fine}$  and the deviation of this correlation from the 1:1 line predicted by spatial scaling. Because  $K_{2,coarse}$  and  $K_{2,fine}$  share a common dependence on the variance of the soil moisture field at scales coarser than 6400 m, statistical interpretation of this correlation is difficult. As a consequence, further analysis centered on the evolution of the relationship between  $K_{2,coarse}$  and  $K_{2,fine}$  as backscatter imagery was processed into estimates of soil moisture, through the intermediate step of soil dielectric. Scatterplots of  $K_{2,coarse}$  versus  $K_{2,fine}$ , analogous to those shown in Figure 12, were constructed for the following fields along the transect:  $\sigma_{HH}$  and  $\sigma_{VV}$  backscatter (Figure 10), soil dielectric (Figure 11), soil moisture based on the *Brisco et al.* [1992] model (Figure 12a), and soil moisture derived from the *Hallikainein et al.* [1985] model (Figure 12b).

For each scatterplot the following ratio was calculated

$$\frac{\sum (\hat{K}_{2,fine} - K_{2,fine})^2}{\sum (K_{2,fine} - \bar{K}_{2,fine})^2}, \quad (24)$$

where  $\hat{K}_{2,fine}$  and  $\bar{K}_{2,fine}$  are the predicted and mean observed values for the fine-scale scaling exponent along the length of the transect. The spatial scaling model predicts a value of  $K_{2,fine}$  equal to  $K_{2,coarse}$ . The ratio defined in (24) is a normalized measure of the error associated with the spatial scaling model and assesses the ability of a downscaling model, based on spatial scaling, to accurately predict  $K_{2,fine}$  given  $K_{2,coarse}$ . Figure 13a plots values of this ratio for each of the processing steps. The increase in the normalized error, from the radar backscatter data (left two points) into soil dielectric and then soil moisture (right two points), suggests that the estimation of the soil moisture field is associated with a reduction in the predictive ability of the spatial scaling model.

Figures 13b and 13c plot  $r^2$  values and slopes estimated from fitting linear regressions to the scatterplots shown in

Figures 10, 11, and 12. The spatial scaling model predicts a slope of 1.0 for this relationship. Figure 13b demonstrates that processing of radar backscatter into soil moisture estimates results in fields that deviate from this prediction. But, as shown in Figure 13c, the strength of the correlation between  $K_{2,fine}$  and  $K_{2,coarse}$  appears to increase during processing.

## 6. Conclusions

Results suggest that the coarse-scale (800 to 6400 m) correlation structure of volumetric soil moisture fields can be related to statistics observed at finer (100 to 800 m) scales. However, the form of the relationship does not conform to a

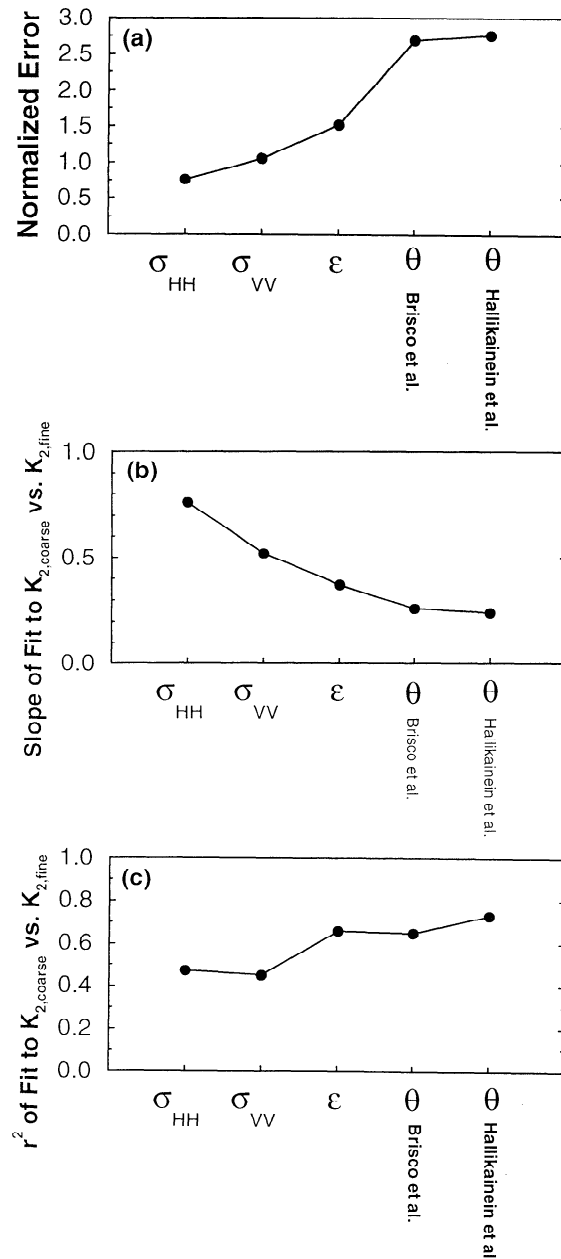


**Figure 13.** Measured values of (a) the normalized error, see (24), associated with the spatial scaling model, (b) fitted slope, (c) and  $r^2$  for scatterplots shown in Figures 10, 11, and 12.

spatial scaling model. In fact, the predictive power of the spatial scaling model is reduced when backscatter images are processed into estimations of soil moisture (Figure 13a). Two alternative features are attributed to the scaling behavior of soil moisture fields between 800 and 6400 m: the presence of a correlation between fine- and coarse-scale scaling exponents (Figure 13c) and the deviation of this correlation from the 1:1 line predicted by spatial scaling (Figure 13b). Both of these attributes emerge as backscatter fields are processed into estimates of soil moisture, through the intermediate step of estimating soil dielectric. These results suggest that a robust downscaling procedure, applied to soil moisture over these length scales (100 to 6400 m), will require a more complicated description of the relationship between  $K_{2, \text{fine}}$  and  $K_{2, \text{coarse}}$  than the 1:1 assumption made by the spatial scaling model.

Clearly errors exist in the estimated soil moisture imagery. The lack of temporal coverage makes it difficult to completely filter the effects of static (i.e., nonsoil moisture) sources of variability. Topography, soil texture, and vegetation are all capable of introducing spurious variability into soil moisture maps derived from SIR-C data. To what degree these sources of error affect the soil moisture scaling attributes noted in the previous paragraph is difficult to quantify. However, the fact that these attributes emerge as the soil moisture signal is gradually isolated during processing suggests that they are true expressions of soil moisture variability.

The long transect used in this analysis is a critical component for understanding the scaling behavior of soil moisture fields. The large domain size (200 km) combined with the fine resolution (25 m) provides a rare look at the scaling behavior of soil moisture fields at scales that span the gap between typical in situ investigations (~100 m) and the resolution of next generation microwave remote sensors (10 to 50 km). The large domain size also makes it possible to analyze soil moisture fields under a variety of topographic, vegetative, and hydrologic conditions. The transect examined here, for example, crosses a steep gradient in antecedent rainfall accumulations (see Figure 2b).

Further work should be based on repeated imaging of the same landscape over a broad range of hydrologic conditions. Complete validation of these results will also require comparisons of soil moisture scaling behavior measured using a variety of observational and computational tools (e.g., in situ, passive microwave, active microwave, and hydrologic modeling). The data sets for such a complete analysis do not exist yet. Until they do, analysis of the April 1994 SIR-C data set provides a valuable first look at soil moisture scaling properties in the southern Great Plains.

**Acknowledgments.** This research was supported in part through NASA grants NAG8-1517 and NAG5-6494. The authors would like to thank Ann Y. Hsu for her revision suggestions and the Earth Science Center at Pennsylvania State University for providing the STATSGO soil texture imagery.

## References

- Avissar, R., Conceptual aspects of a statistical-dynamic approach to represent landscape subgrid-scale heterogeneities in atmospheric models, *J. Geophys. Res.*, **97**, 2729-2742, 1992.
- Avissar, R., and R.A. Pielke, A parameterization of heterogeneous land surface for atmospheric numerical models and its impact on regional meteorology, *Mon. Weather. Rev.*, **117**, 2113-2136, 1989.
- Blöschl, G., and M. Sivipalan, Scale issues in hydrological modeling: A review, in *Scale Issues in Hydrological Modeling*, edited by M. Sivipalan and J.D. Kalma, pp. 9-48, John Wiley, New York, 1995.
- Brisco, B., T.J. Pultz, R.J. Brown, G.C. Topp, M.A. Hares, and W.D. Zebchock, Soil moisture measurement using portable dielectric probes and time domain reflectometry, *Water Resour. Res.*, **28**, 1339-1346, 1992.
- Dubayah, R., E.F. Wood, and D. Lavellée, Multiscaling analysis in distributed modeling and remote sensing: An application using soil moisture, in *Scale, Multiscaling, Remote Sensing, and GIS*, edited by M.F. Goodchild and D.A. Quattrochi, pp. 93-111, Cambridge Univ. Press, New York, 1996.
- Dubois, P., J. van Zyl, and E.T. Engman, Measuring soil moisture with imaging radars, *IEEE Trans. Geosci. Remote Sens.*, **33**(4), 915-927, 1995.
- Famiglietti, J.S., and E.F. Wood, Multiscale modeling of spatially variable water and energy balance processes, *Water Resour. Res.*, **30**, 3061-3078, 1994.
- Federer, C.A., A soil-plant-atmosphere model for transpiration and the availability of soil water, *Water Resour. Res.*, **15**, 555-562, 1979.
- Gupta, V.K., and E.C. Waymire, Multiscaling properties of spatial rainfall and river distributions, *J. Geophys. Res.*, **95**, 1999-2009, 1990.
- Hallikainen, M.T., F.T. Ulaby, M.C. Dobson, M.A. El-Rayes, and L.K. Wu, Microwave dielectric behavior of wet soil, I, Empirical models and experimental observations, *IEEE Trans. Geosci. Remote Sens.*, **23**(1), 25-34, 1985.
- Houser, P.R., W.J. Shuttleworth, J.S. Famiglietti, H.V. Gupta, K.H. Syed, and D.C. Goodrich, Integration of soil moisture remote sensing and hydrologic modeling using data assimilation, *Water Resour. Res.*, **34**, 3405-3420, 1998.
- Jackson, T.J., Laboratory evaluation of a field portable dielectric/soil moisture probe, *IEEE Trans. Geosci. Remote Sens.*, **28**(1), 148-151, 1990.
- Jackson, T.J., H. McNairn, M.A. Weltz, B. Brisco, and R. Brown, First order surface roughness correction of active microwave observations for estimating soil moisture, *IEEE Trans. Geosci. Remote Sens.*, **35**(4), 1065-1069, 1997.
- Pierce, L.E., F.T. Ulaby, K. Sarabandi, and M.C. Dobson, Knowledge-based classification of polarimetric SAR images, *IEEE Trans. Geosci. Remote Sens.*, **32**(5), 1081-1087, 1994.
- Rodriguez-Iturbe, I., G.K. Vogel, R. Rigon, D. Entekhabi, F. Castelli, and A. Rinaldo, On the spatial organization of soil moisture fields, *Geophys. Res. Lett.*, **22**, 2757-2760, 1995.
- Shi, J.C., J. Wang, A.Y. Hsu, P.E. O'Neill, and E.T. Engman, Estimation of bare surface soil moisture and surface roughness using L-band SAR image data, *IEEE Trans. Geosci. Remote Sens.*, **35**(5), 1254-1265, 1997.
- Ulaby, F.T., G.A. Bradley, and M.C. Dobson, Microwave backscatter dependence on surface roughness, soil moisture, and soil texture, II, Vegetation-covered soil, *IEEE Trans. Geosci. Remote Sens.*, **GE-17**(2), 33-40, 1979.
- Van de Griend, A.A., and M. Owe, Bare soil surface resistance to evaporation by vapor diffusion under semiarid conditions, *Water Resour. Res.*, **30**, 181-188, 1994.
- Wang, J.R., A. Hsu, J.C. Shi, P.E. O'Neill, and E.T. Engman, A comparison of soil moisture retrieval models using SIR-C measurements over the Little Washita River watershed, *Remote Sens. Environ.*, **59**, 308-320, 1997.
- Wood, E.F., Effects of soil moisture aggregation on surface evaporation fluxes, *J. Hydrol.*, **190**, 397-412, 1997.
- Wood, E.F., Scale analysis for land surface hydrology, in *Scale Dependence and Scale Invariance in Hydrology*, edited by G.posito, pp. 1-30, Cambridge Univ. Press, New York, 1998.

W.T. Crow (corresponding author) and E.F. Wood, Department of Civil and Environmental Engineering, Princeton University, Princeton, NJ 08544 (wadecrow@princeton.edu)

R. Dubayah, Department of Geography, University of Maryland, College Park, MD 20742

(Received December 7, 1998; revised September 15, 1999; accepted September 15, 1999.)